



## Article

# Ultraviolet Erythematel Irradiance (UVER) under Different Sky Conditions in Burgos, Spain: Multilinear Regression and Artificial Neural Network Models

S. García-Rodríguez <sup>1</sup>, A. García-Rodríguez <sup>1</sup>, D. Granados-López <sup>1</sup>, I. García <sup>1,2</sup> and C. Alonso-Tristán <sup>1,\*</sup>

- <sup>1</sup> Research Group Solar and Wind Feasibility Technologies (SWIFT), Electromechanical Engineering Department, Universidad de Burgos, Escuela Politécnica Superior, 09006 Burgos, Spain; solgr@ubu.es (S.G.-R.); agrodriguez@ubu.es (A.G.-R.); dgranados@ubu.es (D.G.-L.); ignacio.garcia@unavarra.es (I.G.)
- <sup>2</sup> Institute of Smart Cities (ISC), Engineering Department, Universidad Pública de Navarra, Campus Arrosadía, Pamplona 31006, Spain
- \* Correspondence: catristan@ubu.es or cristinaalonso.tristan@gmail.com; Tel.: +34-947-258853

**Abstract:** Different strategies for modeling Global Horizontal UltraViolet Erythematel irradiance (GHUVE) based on meteorological parameters measured in Burgos (Spain) have been developed. The experimental campaign ran from September 2020 to June 2022. The selection of relevant variables for modeling was based on Pearson's correlation coefficient. Multilinear Regression Model (MLR) and artificial neural network (ANN) techniques were employed to model GHUVE under different sky conditions (all skies, overcast, intermediate, and clear skies), classified according to the CIE standard on a 10 min basis. ANN models of GHUVE outperform those based on MLR according to the traditional statistical indices used in this study ( $R^2$ , MBE, and nRMSE). Moreover, the work proposes a simple all-sky ANN model of GHUVE based on usually recorded variables at ground meteorological stations.



**Citation:** García-Rodríguez, S.; García-Rodríguez, A.; Granados-López, D.; García, I.; Alonso-Tristán, C. Ultraviolet Erythematel Irradiance (UVER) under Different Sky Conditions in Burgos, Spain: Multilinear Regression and Artificial Neural Network Models. *Appl. Sci.* **2023**, *13*, 10979. <https://doi.org/10.3390/app131910979>

Academic Editor: Harry Kambezidis

Received: 15 August 2023  
Revised: 29 September 2023  
Accepted: 2 October 2023  
Published: 5 October 2023



**Copyright:** © 2023 by the authors. Licensee MDPI, Basel, Switzerland. This article is an open access article distributed under the terms and conditions of the Creative Commons Attribution (CC BY) license (<https://creativecommons.org/licenses/by/4.0/>).

**Keywords:** ultraviolet erythematel irradiance; UVER; statistical analysis; modeling; ANN; multilinear regression models

## 1. Introduction

Ultraviolet radiation (UV) represents a small fraction of total solar radiation (5–7%) [1]. It is a highly energetic component of the solar spectrum that must be monitored as it can be detrimental to life on Earth [2], becoming the main risk factor for human health among photo-biological factors [3]. The UV region of the solar spectrum spans wavelengths between 100 and 400 nm, and it is divided into three components, i.e., UVA, UVB, and UVC. Although UVC radiation (100–280 nm) is entirely absorbed by atmospheric oxygen and ozone, a fraction of UVB (280–315 nm) and UVA (315–400 nm) reaches the Earth's surface as ozone partially absorbs these wavelengths [4]. Surface UV is also influenced by geographical parameters like altitude over the sea level and latitude [5].

UV radiation exerts significant effects on biological and photochemical processes [6], showing both beneficial and detrimental impacts. It has beneficial effects on humans, animals, plants, and the biosphere: while moderate doses of UV radiation enhance vitamin D synthesis, promote mental health, and reduce blood pressure [3,7,8], excessive exposure to UV radiation can cause cataracts, premature aging of the skin and skin cancer [1,9–11]. It also has negative effects on organisms, marine and terrestrial ecosystems, and certain building materials (paints and plastics) [12,13]. Ideally, there should be a balance in UV radiation exposure to reduce the adverse effects associated with too few or too high exposures [8].

The impacts of UV radiation on the skin have been commonly assessed using UV erythematel irradiance (UVER). In accordance with the ISO/CIE17166 : 2019(E) standard [14],

UVER is determined by applying a spectral weighting function known as the erythema spectral weighting function. This function quantifies the effectiveness of radiation at each wavelength ( $\lambda$ ) to cause minimal erythema. The UVER value is obtained by weighting the spectral irradiance of the UV radiation at each wavelength using the corresponding erythema effectiveness factor and then summing up these weighted values for all wavelengths present in the source spectrum, as specified in the standard.

Due to the lack of UV and UVER sensors in many ground-based weather stations [15], these variables are often estimated from other radiometric or meteorological parameters. The effect of cloudiness on UVER has been analyzed for all-sky conditions. In overcast conditions and skies with low clouds, UVER decreases as cloudiness increases [16]. Cloud optical thickness and UVER radiation have an exponential dependence, with higher attenuation occurring in low clouds [17]. Therefore, the solar zenith angle ( $\theta_z$ ) is one of the most influential parameters in the variation of UVER [18]. As  $\theta_z$  increases, there is a corresponding decrease in UVER [16,19]. Notably, a reduction of up to 40% is observed when the zenith angle increases from 20° to 50° [19].

The relationship between UVER, relative optical air mass, and atmospheric clearness has been analyzed, concluding that atmosphere transmissivity to UVER exhibits higher sensitivity to changes in atmospheric clearness compared to variations in the total ozone column (TOC) [20].

Previous research has assessed the effect of ozone on UVER, revealing that higher ozone levels lead to a decrease in UVER due to the ozone absorption band within the UV range [18,21]. The dependence of UVER on ozone is influenced by the variation of the zenith angle [13]. The influence of TOC on UVER is considerably smaller under overcast skies than under clear skies [22].

Different mathematical models have been developed to model UVER as a function of different meteorological variables. Empirical and radiative transfer models have been used to correlate UV radiation, solar broadband radiation, and atmospheric parameters (cloudiness, TOC, aerosols) [12,18,19,23–26]. Linear regressions (LR) have analyzed the effect of some geometric and atmospheric parameters on the ratio between global horizontal UV erythemal irradiance (GHUVE) and global horizontal irradiance (GHI). The aerosol load, TOC, and precipitable water exhibit a linear relationship with respect to GHUVE/GHI while  $\theta_z$  and clearness index,  $k_t$ , defined as the ratio of GHI over the corresponding extraterrestrial irradiance, exhibit exponential and polynomial behaviors, respectively [27]. Additionally, LR was employed to analyze the GHUVE/GHI ratio at various altitudes, revealing a strong correlation between these variables. The determination coefficient ( $R^2$ ) exhibits an increasing trend with higher altitudes [12].

In recent years, the use of machine learning (ML) algorithms for modeling climatic and meteorological data has become widespread [28]. These algorithms allow us to solve complex problems with higher performance than classical modeling [29]. Among the ML techniques, Artificial Neural Networks (ANN) are particularly noteworthy as they act as “black boxes” that establish mathematical relationships between the inputs and the output data without prior knowledge of the specific relationship (linear or nonlinear) existing between them [30]. Numerous researchers have used ANNs to calculate UVER, using GHI as main input [31–36] regardless of the characteristics of the other variables used. Table 1 shows an overview of the variables used in different studies to estimate UVER and the ratio UVER/GHI from ANN, LR, and multilinear regressions (MLR). Notably, GHI and TOC [31,34–36] have been used as the most used inputs in conjunction with other variables in all cases.

**Table 1.** Studies to estimate UVER ratio around the world.

Ref.	Location	Model	Meteorological Variables	Models	Data Granularity
[37]	Spain	UVER	$m$ , TOC, VIS, latitude, cloudiness	ANN	3 h
[31]	Spain	UVER	$m$ , TOC, $k$ , $k_b$ , $k_t$	ANN	30 min
[38]	Spain	UVER	TOC, cloudiness, AOD	MLR	1 min
[27]	Thailand	UVER/GHI	$\theta_z$ , AOD, TOC, $k_t$ , precipitable water	LR	10 min
[39]	Korea	UVER/GHI	CC, AOD, SCD	MLR	10 min
[40]	Spain	UVER	$m$ , TOC, $k_t$	LR	30 min
[34]	Germany	UVER	GHI, DHI, SD, TOC, VIS, $\theta_z$	ANN	daily
[35]	European Sites	UVER/GHI	SD, GHI, DHI, $\theta_z$ , CC, TOC, VIS, Month, snow weight, Albedo.	ANN	30 min
[36]	Serbia	UVER	GHI, cloudiness, $m$ , $k_t$ , TOC	ANN	10 min
[12]	Argentina	UVER/GHI	GHI, $\theta_z$ , $k_t$ , altitude	LR	1 min

$m$  : relative optical air mass, TOC: total ozone column, VIS: horizontal visibility, SCD : ozone slant column density,  $\theta_z$ : solar zenith angle, AOD: aerosol optical depth, CC: cloud cover, GHI: global irradiation, DHI: diffuse irradiation, SD: sunshine duration

The main objective of this work is to develop mathematical models using different strategies for UVER from meteorological parameters measured in Burgos (Spain) during an extensive experimental campaign run from September 2020 to June 2022. After selecting the variables based on the Pearson correlation coefficient, both MLR and ANN techniques were employed to model GHUVE under different sky conditions, including all skies, overcast, intermediate, and clear skies, classified according to ISO/CIE standard sky classification [41]. It is important to highlight that the variables used in the models developed in this study were experimental variables typically recorded in terrestrial facilities that underwent the strictest quality controls. The use of variables from satellite observations or additional databases was discarded due to their different sampling frequency and to guarantee, as far as possible, the applicability of locally obtained models in other emplacements using only ground meteorological data.

The work is structured as follows: in Section 2, the experimental data used for modeling are described and analyzed, along with the criteria ensuring their quality. Section 3 presents the feature selection process based on the Pearson criterion. A complete discussion of the results is shown in Section 4. Finally, Section 5 presents the key findings and main conclusions obtained from this study.

## 2. Experimental Data and Quality Control

The SWIFT Research Group ground meteorological facility, located on the flat roof of the Higher Polytechnic School of the University of Burgos (42°21'04" N, 3°41'20" W, 856 m a.s.l.), and shown in Figure 1, has provided the experimental data used for this study, in a 10 min basis, with an average scanning granularity of 30 s, recorded from September 2020 to June 2022.

Various climatic parameters were recorded, including air temperature (T), relative humidity (RH), wind speed (WS), and direction. GHI and Diffuse Horizontal Irradiance (DHI) were measured with Hukseflux pyranometers (model SR11) and Direct Normal Irradiance (DNI) by means of a Hukseflux pyrliometer (model DR01). A GEONICA-SEMS-3000 sun tracker equipped with a shading disc was employed for the measurement of DHI. Additionally, the pyrliometer was mounted on the sun tracker to measure DNI. GHUVE values were obtained with a Kipp and Zonnen SUV-E radiometer. Sky luminance and radiance distributions, used to classify the sky condition, were determined with a sky-scanner EKO MS-321LR. The cloud cover (CC) was calculated with a commercial all-sky camera (SONAD201D) that records every 1 s an RGB color image with 1158 × 1172 pixels of resolution. A complete description of the experimental facility and instruments can be found in previous works [42,43].

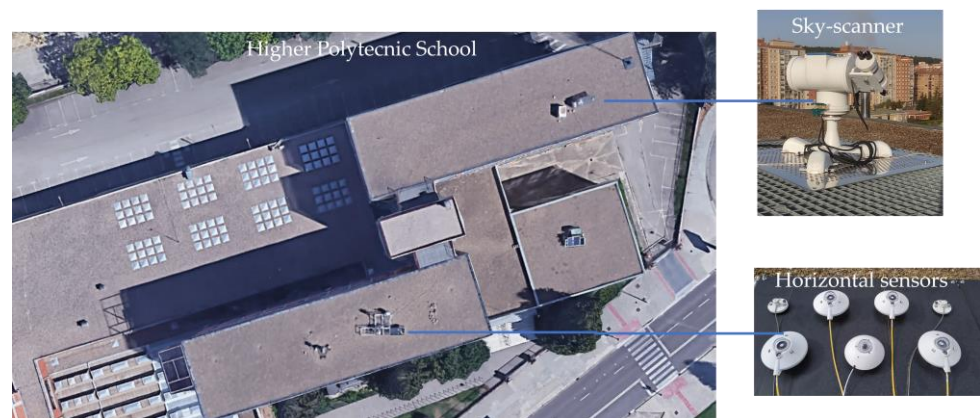


**Figure 1.** Experimental facility used in this study (Higher Polytechnic School, University of Burgos, Spain).

The collected GHI, GHUVE, DHI, and DNI data underwent the quality control procedure recommended by the MESoR project [44]. For the GHUVE data, it was determined that GHUVE values should not exceed the corresponding extraterrestrial UVER on the horizontal plane ( $UVEH_0$ ). The calculation of  $UVEH_0$  involved applying a correction factor ( $f_c$ ), which considered the estimated orbital eccentricity to the UVER solar constant ( $UVE_{sc}$ ) multiplied by the cosine of the solar zenith angle ( $\theta_z$ ), as described in Equation (1).

$$UVEH_0 = f_c \cdot UVE_{sc} \cdot \cos \theta_z \quad (1)$$

In the absence of a standardized value,  $UVE_{sc}$  was determined by integrating the product of the extraterrestrial solar spectrum [45] and the erythema spectral weighting function [14] over the wavelength range of 280 to 400 nm. This calculation yielded a value of  $14.5 \text{ W} \cdot \text{m}^{-2}$ . Data points corresponding to solar elevation angles below  $5^\circ$  were excluded from the analysis to mitigate the cosine response issues inherent to the GHI, and GHUVE measurement instruments.

A summary of the variables used in this study is shown in Table 2. Among these meteorological variables, the following were directly obtained from the experimental measurements: GHI, DHI, DNI, CC, RH, T, and WS.  $\theta_z$ , and  $\psi$  were calculated. The remaining variables, including diffuse fraction,  $D$  [46],  $k_t$  [47],  $k'_d$ , Perez's brightness factor ( $\Delta$ ) [48], and Perez's clearness index,  $\varepsilon$  [48], were calculated using the equations described in Table 2.

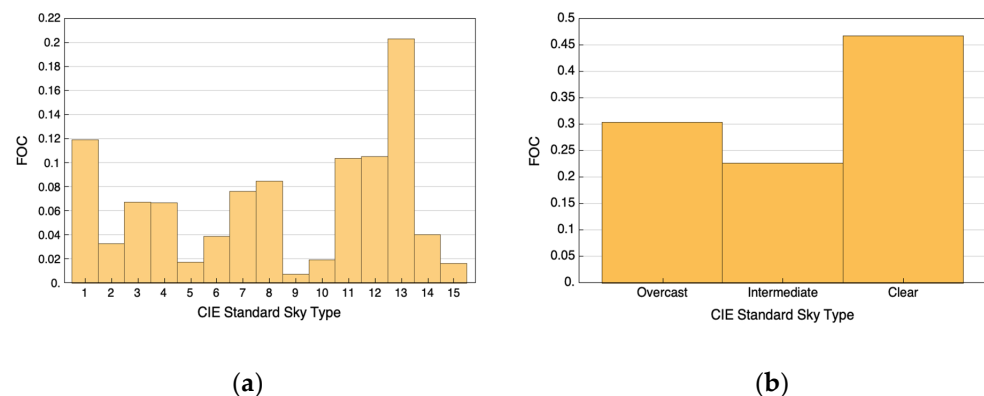
The skies of the city of Burgos have been classified according to the ISO/CIE standard [41], which considers the angular distribution of luminance in the sky measured by the sky scanner. The sky is classified into 15 different types, where types 1 to 5 are considered overcast skies, types 6 to 10 are categorized as intermediate skies, and sky types 11 to 15 are identified as clear skies. A complete description of the ISO/CIE classification according to 15 types based on sky scanner measurements can be found in previous works [42,43].

Figure 2a illustrates the frequency of occurrence (FOC) of each ISO/CIE standard sky type during the experimental campaign. Clear skies predominate in Burgos, with the most frequent sky type being classified as 13 (cloudless polluted with a wider solar corona). This sky type exceeds the 20% of all observed skies. When only the three main sky categories are considered, as shown in Figure 2b (overcast, intermediate, and clear), clear skies have the highest FOC (higher than 45%). This fact concurs with findings from previous studies conducted in Burgos [28].

**Table 2.** Variables measured and calculated in Burgos.

Variables.	Meteorological Variables	Expression
GHI	Global Horizontal irradiance	measured
DHI	Diffuse Horizontal irradiance	measured
DNI	Direct Normal irradiance	measured
CC	Cloud cover	measured
RH	Relative Humidity	measured
T	Air temperature	measured
WS	Wind speed	measured
$\psi$	Solar azimuth angle	calculated
$\theta_z$	Solar zenith angle	calculated
D	Diffuse fraction	$D = \frac{DHI}{GHI}$
$k_t$	Clearness index	$k_t = \frac{GHI}{B_{sc} \cdot f_c \cdot \cos \theta_z}$
$k_d$	Diffuse to extraterrestrial irradiance	$k_d = \frac{DHI}{B_{sc}}$
$\Delta$	Perez’s brightness factor	$\Delta = \frac{m \cdot DHI}{B_{sc} \cdot f_c \cdot \cos \theta_z}$
$\epsilon$	Perez’s clearness index	$\epsilon = \frac{DHI + DNI}{DHI} + k(\theta_z)^3$

$B_{sc}$  is the solar constant ( $1361.1 \text{ W}\cdot\text{m}^{-2}$  [49]).  $f_c$  is the average value of the orbital eccentricity of the Earth.  $k = 1.04$  (or  $5.56 \cdot 10^{-6}$  if  $\theta_z$  is expressed in degrees).



**Figure 2.** Frequency of occurrence (FOC) in Burgos (Spain) (a) of each ISO/CIE standard sky type, and (b) for each ISO/CIE sky type group.

The box and whisker plot of Figure 3 shows the distribution of the GHUVE/GHI ratio based on 10 min data grouped by UTC hours, calculated from sunrise to sunset, using the complete database of the experimental campaign. The graph presents various statistical measures, including the mean value (gray crosses), the median (white lines inside the box), the interquartile range (the limits of the boxes), and both the maximum and minimum data values (the extreme whiskers), as well as the outlier values (black and gray circles). It can be observed that the hourly mean and median values of GHUVE/GHI gradually increased until noon (12 : 00 h) and then decreased until sunset. Higher dispersion of the values in the central hours of the day (10 : 00 h to 14 : 00 h) may be observed, as shown by the interquartile range (around  $9 \cdot 10^{-3}\%$ ). The maximum value ( $4.2 \cdot 10^{-2}\%$ ) is reached at 12 : 00 h UTC.

Figures 4 and 5 show the statistical analysis of the 10 min data of the GHUVE/GHI ratio grouped by month and season, respectively. Figure 4 reveals a gradual increase of GHUVE/GHI until May, followed by practically constant values until August, and then a decrease for the rest of the year. The interquartile range fluctuated between  $3 \cdot 10^{-3}\%$  and  $1.2 \cdot 10^{-2}\%$  and the standard deviation ranged between  $3 \cdot 10^{-3}\%$  and  $7 \cdot 10^{-3}\%$ . During the months from May to August, the ratio exhibited the greatest dispersion of the measurement campaign, with interquartile ranges around  $1.1 \cdot 10^{-2}\%$  and standard



deviations around  $6 \cdot 10^{-3}\%$ . The maximum value was recorded in July ( $4.2 \cdot 10^{-2} \cdot \%$ ), while the minimum was reached in April ( $1 \cdot 10^{-3}\%$ ).

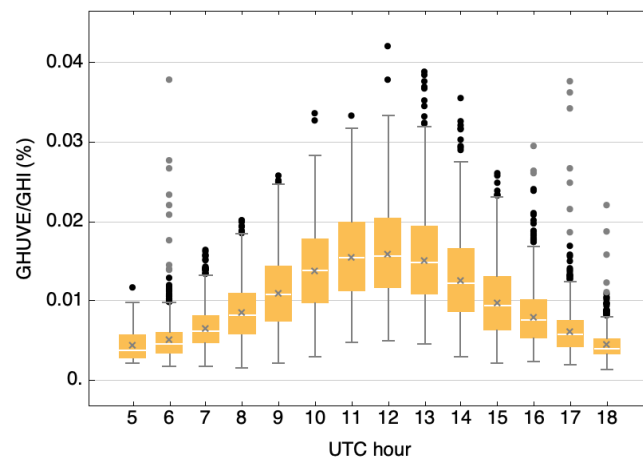


**Figure 3.** Box and whisker plot of the GHUVE/GHI ratio based on 10 min data grouped by UTC hours. Gray crosses indicate the mean, and the white lines inside the box indicate the median. The limits of the boxes define the first, second, and third quartiles, whereas the extreme whiskers show the minimum and the maximum points. Black and gray circles represent outliers.

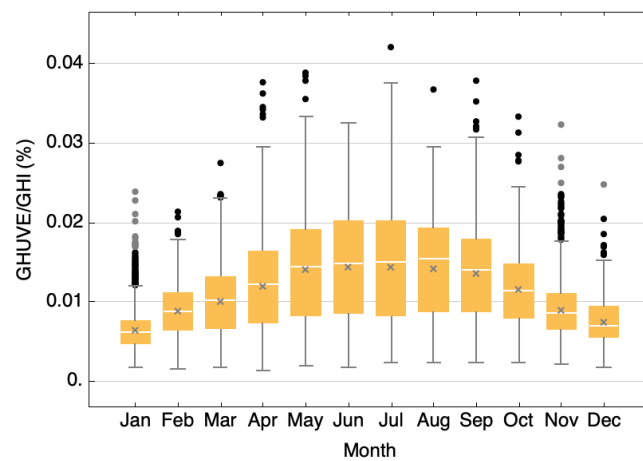


**Figure 4.** Box and whisker plot of the GHUVE/GHI ratio based on 10 min data grouped by months.

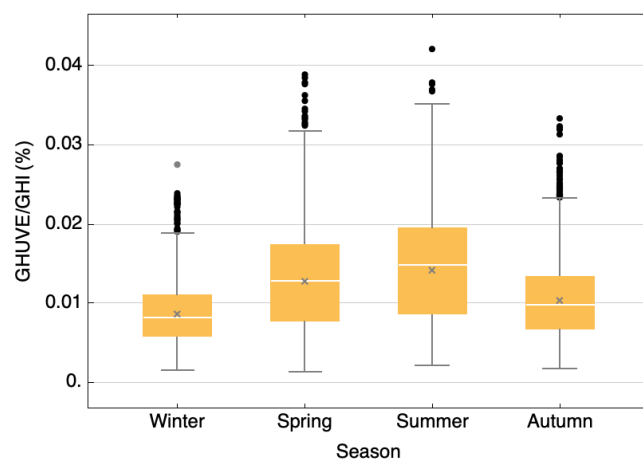


**Figure 5.** Box and whisker plot of the GHUVE/GHI ratio based on 10 min data grouped by seasons.

Figure 5 shows the greatest dispersion of values for the summer months and the highest value of the GHUVE/GHI ratio. Conversely, the dispersion of values in winter was relatively smaller. The interquartile ranges were  $1.1 \cdot 10^{-2}\%$  and  $5 \cdot 10^{-3}\%$  with standard deviations of  $6 \cdot 10^{-3}\%$  and  $4 \cdot 10^{-3}\%$ , respectively.

Upon analyzing the GHUVE/GHI ratio based on the 15 ISO/CIE sky types (Figure 6), it is evident that sky type 15 exhibits the highest ratio value and the lowest data dispersion. Conversely, sky type 12 demonstrates the lowest ratio value, with an average level of data dispersion. Notably, both sky types belong to the category of clear skies.

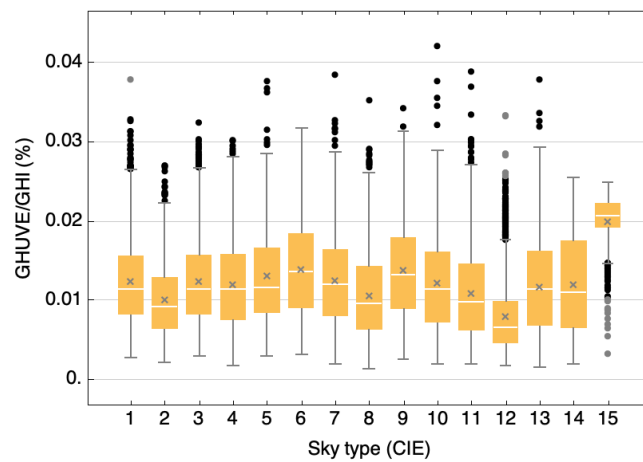


Figure 6. Box and whisker plot of the GHUVE/GHI standard sky type (1 to 15).

Figure 7 shows that the variation between the mean ( $1.1 \cdot 10^{-2} - 1.2 \cdot 10^{-2}\%$ ) and the dispersion (interquartile range:  $8 \cdot 10^{-3} - 9 \cdot 10^{-3}\%$ , standard deviation:  $5 \cdot 10^{-3} - 6 \cdot 10^{-3}\%$ ) of the three main ISO/CIE sky types is very similar.

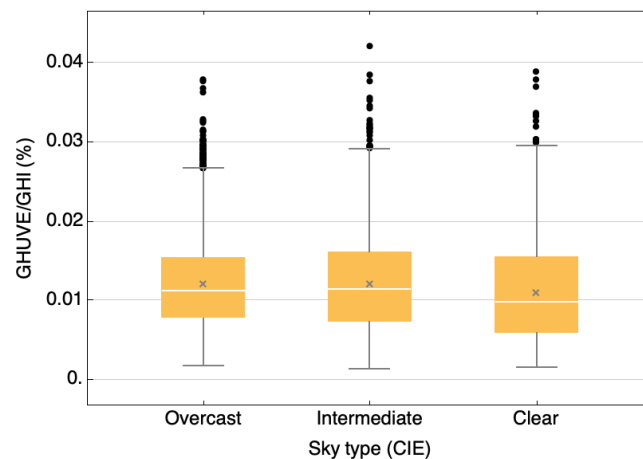


Figure 7. Box and whisker plot of the GHUVE/GHI ratio based on 10 min data grouped by sky type group (overcast, intermediate, clear).

### 3. Methodology

#### 3.1. Feature Selection

Feature selection (FS) identifies the features that are related within a dataset, and it allows the elimination of irrelevant or unimportant features that contribute little or nothing to the definition of the target variable, providing more accurate models. This technique increases the performance of the developed model, improving its accuracy and reducing its complexity and overfitting, as well as its execution time.

In this study, to determine the most relevant meteorological variables for the estimation of UVER, a selection of variables was performed based on the Pearson correlation

coefficient ( $r$ ), and the following rules: if GHUVE and one selected variable have a very weak relationship, the Pearson coefficient is 0; the relationship is very strong when  $r$  is close to 1 (direct correlation) or  $-1$  (inverse correlation). To facilitate the assessment of correlation strength, the Thumb rule [50] established five  $r$  intervals for the correlation: direct ( $1 \geq |r(\text{GHUVE, variable})| \geq 0.9$ ), strong ( $0.9 > |r(\text{GHUVE, variable})| \geq 0.7$ ), moderate ( $0.7 > |r(\text{GHUVE, variable})| \geq 0.5$ ), weak ( $0.5 > |r(\text{GHUVE, variable})| \geq 0.3$ ), and negligible ( $|r(\text{GHUVE, variable})| < 0.3$ ).

Table 3 shows the various intervals of Pearson’s coefficients calculated for the different meteorological variables. It can be observed that GHI exhibits a very strong and direct influence on GHUVE for all-skies, overcast, and clear skies, while for intermediate skies, GHI is strongly correlated. In clear skies,  $\theta_z$  is also very strong and is inversely correlated with GHUVE, while for all-skies, overcast, and intermediate skies, this variable is strongly correlated. Likewise, in the case of all-sky types,  $k_t$ ,  $D$ ,  $\epsilon$ , RH, DNI, and T have a moderate relationship with GHUVE. When analyzing overcast skies, a direct and strong relationship with  $k_d$  and DHI is observed, and a moderate relation with  $k_t$ ,  $D$ ,  $\Delta$ , DNI. For intermediate skies, the relation between GHUVE and  $k_t$ ,  $k_d$ ,  $D$ , DHI, and DNI is moderate. WS,  $\psi$ , and CC present a negligible relation with GHUVE, so these meteorological variables were discarded as inputs for modeling GHUVE. These findings agree with the literature, which identifies GHI and  $\theta_z$  as the two variables that strongly influence GHUVE measurements [18,19,31]. Meteorological variables whose relationship with GHUVE is moderate, strong, or very strong ( $r \geq 0.5$ ) have been selected.

**Table 3.** Pearson’s coefficients were calculated for the different variables.

CIE Sky Type	$ r(\text{GHUVE,Variable}) $ .				
	[1–0.9]	(0.9–0.7]	(0.7–0.5]	(0.5–0.3]	(0.3,0]
All-sky	GHI	$\theta_z$	$k_t$ , $D$ , $\epsilon$ , RH, DNI, T	$k_d$ , DHI	$\Delta$ , WS, $\psi$ , CC
Overcast	GHI	$\theta_z, k_d$ , DHI	$k_t$ , $D$ , DNI, $\Delta$ ,	$\epsilon$ , RH, T	WS, $\psi$ , CC
Intermediate	-	GHI, $\theta_z$	$k_t$ , $k_d$ , $D$ , DHI, DNI	$\epsilon$ , RH, T	$\Delta$ , WS, $\psi$ , CC
Clear	GHI, $\theta_z$	-	T	$k_t$ , $k_d$ , $D$ , $\epsilon$ , RH, DNI	$\Delta$ , DHI, WS, $\psi$ , CC

### 3.2. Multilinear Regression Model

Meteorological variables selected in Section 3.1 were used as input variables for both MLR and ANN models. Four MLR models were developed: one for all skies and three additional specific models for the clear, intermediate, and overcast sky types. To develop the MLR models, the data were divided into two groups: the first group, comprising 85% of the data, was used for model fitting, and the remaining 15% of the data was used for model validation. Conventional statistics were employed to evaluate the adequacy of fit for each model: coefficient of determination ( $R^2$ ), normalized root mean square error (nRMSE) and normalized mean bias error (nMBE), calculated by Equations (2)–(4), respectively.

$$R^2 = \frac{\sum_{i=1}^n (\text{GHUVE}_{\text{mod}} - \overline{\text{GHUVE}}_{\text{mod}}) \cdot (\text{GHUVE}_{\text{exp}} - \overline{\text{GHUVE}}_{\text{exp}})}{\sqrt{\sum_{i=1}^n [(\text{GHUVE}_{\text{mod}} - \overline{\text{GHUVE}}_{\text{mod}})^2 \cdot (\text{GHUVE}_{\text{exp}} - \overline{\text{GHUVE}}_{\text{exp}})^2]}} \quad (2)$$

$$\text{nRMSE} = \frac{1}{\overline{\text{GHUVE}}_{\text{exp}}} \sqrt{\frac{\sum_{i=1}^n (\text{GHUVE}_{\text{mod}} - \text{GHUVE}_{\text{exp}})^2}{n}} \cdot 100(\%) \quad (3)$$

$$\text{nMBE} = \frac{1}{\overline{\text{GHUVE}}_{\text{exp}}} \frac{\sum_{i=1}^n (\text{GHUVE}_{\text{mod}} - \text{GHUVE}_{\text{exp}})}{n} \cdot 100(\%) \quad (4)$$



where  $n$  represents the number of experimental data points used for model fitting and testing in each case;  $\text{GHUVE}_{\text{exp}}$  is the experimental value of GHUVE, and  $\text{GHUVE}_{\text{mod}}$  is the modeled GHUVE value.

The mathematical expressions of the four regression models and the goodness of fit of each one are shown in Table 4. The model’s fitting results presented a high determination coefficient with the experimental data ( $R^2 > 0.92$ ); however, the nRMSE values obtained through multilinear regressions exceeded 20% in all cases.

**Table 4.** Multilinear regression (MLR) models of GHUVE and goodness of fit (based on 85% of data).

Sky Types	MLR Model	$R^2$	nRSME(%)	nMBE (%)
All skies	$\text{GHUVE} = 1.90 \cdot 10^{-2} + 2.35 \cdot 10^{-4} \text{GHI} - 1.74 \cdot 10^{-2} \theta_z - 9.85 \cdot 10^{-2} k_t + 7.44 \cdot 10^{-4} T$	0.937	25.60	$-2.05 \cdot 10^{-1212}$
Overcast	$\text{GHUVE} = 2.98 \cdot 10^{-2} + 1.61 \cdot 10^{-4} \text{GHI} - 2.71 \cdot 10^{-2} \theta_z + 1.30 k_d - 9.89 \cdot 10^{-4} \text{DHI}$	0.926	29.80	$6.92 \cdot 10^{-13}$
Intermediate	$\text{GHUVE} = 8.54 \cdot 10^{-2} + 2.59 \cdot 10^{-4} \text{GHI} - 6.98 \cdot 10^{-2} \theta_z - 1.80 \cdot 10^{-4} \text{DHI} - 9.91 \cdot 10^{-5} \text{DNI}$	0.934	22.49	$3.23 \cdot 10^{-12}$
Clear	$\text{GHUVE} = 1.75 \cdot 10^{-1} + 5.84 \cdot 10^{-5} \text{GHI} - 1.52 \cdot 10^{-1} \theta_z + 6.89 \cdot 10^{-4} T$	0.940	21.10	$9.87 \cdot 10^{-13}$

### 3.3. Artificial Neural Network Model

In this work, ANNs were used to estimate GHUVE through the Levenberg–Marquardt Back-Propagation (LMBP) algorithm. The ANN architecture adopted for this purpose consists of a single hidden layer and a single output, as outlined in a previous publication [28,29]. In the input layer, each neuron is a meteorological variable. Determining the optimal number of neurons in the hidden layer is currently unknown, but it is acknowledged that this number should not exceed the number of neurons in the preceding layer [51]. Therefore, if the input layer has only one variable and thus a single neuron, the hidden layer can have only one neuron. If the input layer has two meteorological variables, the hidden layer can have either one or two neurons. Similarly, if the input has three variables and, therefore, three neurons, the hidden layer can have three, two, or one neuron/s, and this trend continues for additional variables in the input layer. The iterative process and the fitting are explained elsewhere [28].

Four ANN models were generated and tested in this work, one for all skies and three for each sky type (clear, intermediate, and overcast), considering the selected meteorological variables shown in Table 3. Table 5 shows the goodness of fit for each ANN model according to the described statistics. It can be observed that in four cases, a good determination coefficient was obtained,  $R^2 > 0.95$ . The nRMSE obtained varied between 11.9% and 21.3%. The best results were obtained for clear skies ( $R^2 > 0.98$  and  $\text{nRMSE} < 12\%$ ).

**Table 5.** Goodness of fit of the ANN models (based on 85% of data).

Sky Condition	$R^2$	nRMSE (%)	nMBE (%)
All skies (MLR1)	0.988	14.36	$6.69 \cdot 10^{-2}$
Overcast	0.962	21.32	$6.69 \cdot 10^{-2}$
Intermediate	0.955	18.68	$9.09 \cdot 10^{-2}$
Clear	0.981	11.92	$7.59 \cdot 10^{-3}$

## 4. Results and Discussion

The remaining 15% of the data, not used previously for generating the MLR and ANN models, were used as a validation set for both MLR and ANN models. The results are shown in Table 6, with MLR outcomes on the left and ANN results on the right. The best results were obtained for clear skies ( $R^2 > 0.97$ , and  $\text{nRMSE} < 12.4\%$ ). Both nRMSE and nMBE values obtained through multilinear regressions exceeded 20% in all cases, results

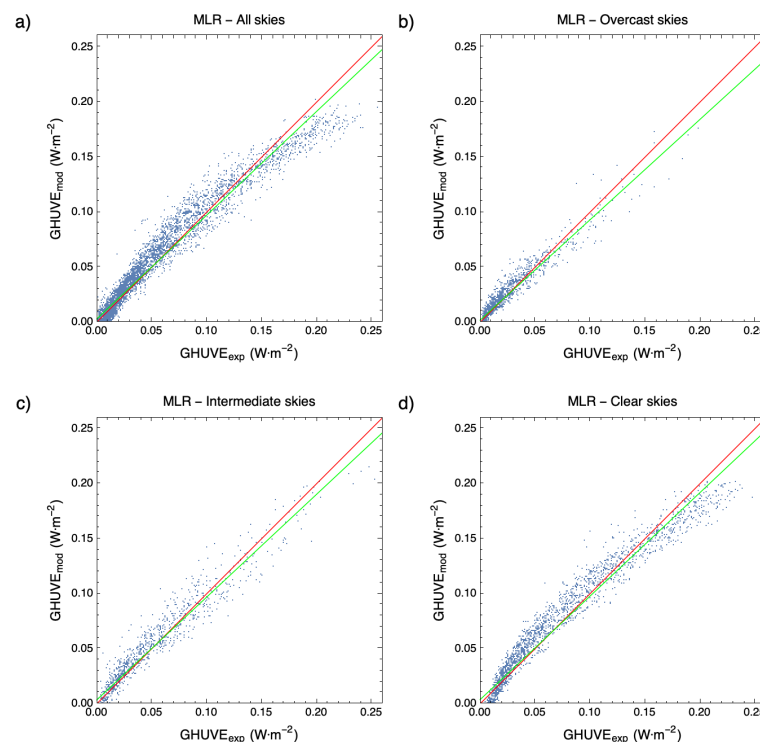
close to those obtained by other authors [2] who performed models using second-degree polynomials, obtaining nRMSE values between 20% and 54%. Previous works modeled hourly [31] and daily [34–37] GHUVE values through ANN obtaining nRMSE ranging from 14 and 21%. Considerable improvement in performances occurred when the highly influential parameter TOC was introduced as ANN input.

**Table 6.** Goodness of fit of MLR and ANN models (based on 15% of data).

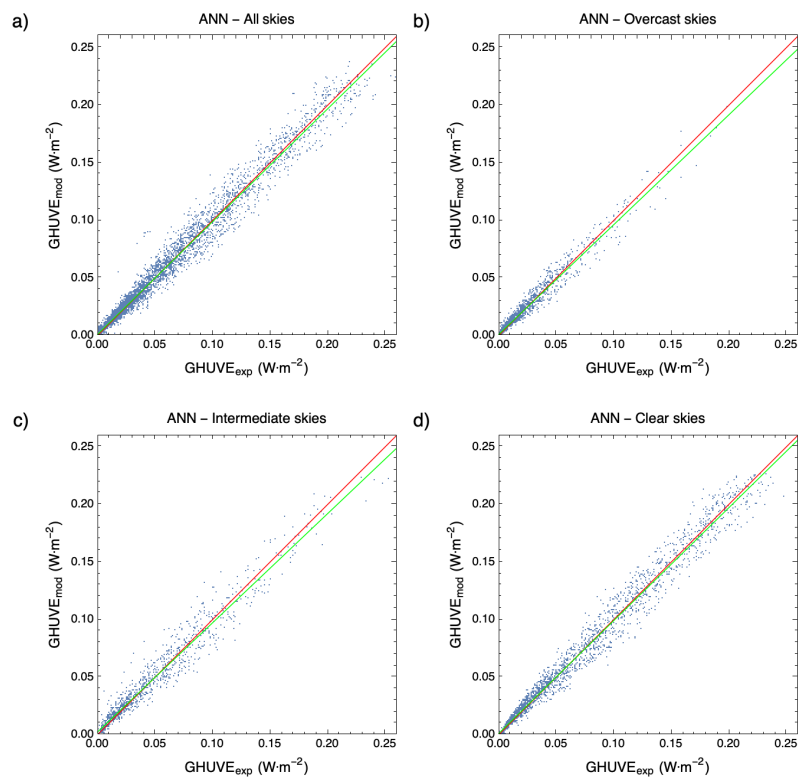
Sky Condition	R <sup>2</sup>	nRSME (%)	nMBE (%)	Sky Condition	R <sup>2</sup>	nRSME (%)	nMBE (%)
All skies (MLR1)	0.938	25.21	1.41 · 10 <sup>-1</sup>	All skies (ANN1)	0.979	14.63	1.55 · 10 <sup>-1</sup>
Overcast (MLR2)	0.930	29.65	6.28 · 10 <sup>-1</sup>	Overcast (ANN2)	0.965	21.06	6.58 · 10 <sup>-1</sup>
Intermediate (MLR3)	0.923	23.57	-5.75 · 10 <sup>-1</sup>	Intermediate (ANN3)	0.953	19.20	3.38 · 10 <sup>-1</sup>
Clear (MLR4)	0.942	20.57	-2.10 · 10 <sup>-1</sup>	Clear (ANN4)	0.979	12.35	4.31 · 10 <sup>-1</sup>

Table 6 comparison revealed that ANN models performed better than MLR models. For all skies and clear skies, the nRMSE value improved significantly, decreasing over 40% with respect to the MLR models. The nMBE value was overestimated for intermediate and clear skies.

Figures 8 and 9 compare the modeled GHUVE values from derived MLR models and ANN models, respectively, and the corresponding experimental GHUVE measurements obtained from the Burgos meteorological station using the referred validation data set. A good determination coefficient was obtained (R<sup>2</sup> > 0.92, MRL models, R<sup>2</sup> > 0.95 ANN models) both for all skies, overcast, intermediate, and clear sky conditions.



**Figure 8.** Comparison between calculated (GHUVE<sub>mod</sub>) from MLR models and experimental GHUVE<sub>exp</sub> data under different sky conditions: (a) all skies, (b) overcast, (c) partial, and (d) clear skies. The green line represents the fitting line; the red line represents the x = y line.



**Figure 9.** Comparison between calculated ( $\text{GHUVE}_{\text{mod}}$ ) from ANN models and experimental  $\text{GHUVE}_{\text{exp}}$  data under different sky conditions: (a) all skies, (b) overcast, (c) partial, and (d) clear skies. The green line represents the fitting line; the red line represents the  $x = y$  line.

To improve the previous results, a new approach was introduced to optimize the number of variables for minimizing nRMSE using ANN models for all-sky conditions. The number of neurons in the hidden layer can be adjusted accordingly to accommodate the complexity and dimensionality of the input data, from one neuron to the number of input variables of the ANN.

The two variables identified as strongly correlated to GHUVE based on Pearson’s coefficient, as shown in Table 3, GHI and  $\theta_z$ , were used as reference in this study. The ANN with two neurons in the hidden layer, with GHI and  $\theta_z$  as input variables presented nRMSE of 17.02%, as shown in Table 7. By retaining GHI and  $\theta_z$  as input variables, new ANN models were generated, increasing one by one the number of variables included in Table 2 and, consequently, the number of neurons in the hidden layer, from one neuron to as many neurons as the number of variables in each case.

**Table 7.** nRMSE for ANN model (GHI,  $\theta_z$ ) calculated with one and two neurons.

All-Skies	nRMSE(%)	
	One neuron	Two neurons
GHI, $\theta_z$	18.65	17.02

Table 8 shows the percentage of GHUVE ANN models resulting from combinations of input variables out of the total of possible combinations for each case, whose nRMSE was below 15%. For the combination of five variables, with two to five neurons in the hidden layer, nRMSE < 15% was obtained for 5%, 25%, 28%, and 30% of the generated ANNs, respectively. For the combination of six variables, from two neurons to six neurons, nRMSE < 15% was obtained for the range 22 – 57% of the generated ANN models.

**Table 8.** Percentage of generated GHUVE ANN models, according to number of input variables and number of neurons, with nRSME < 15%..

Number of neurons in the hidden layer	Number of Input Variables			
	3	4	5	6
1	0	0	0	0
2	0	2	5	22
3	8	14	25	27
4		18	28	41
5			30	48
6				57

Table 9 shows the combinations of five and six input variables ranging from two to six neurons in the ANN hidden layer, which estimated the lowest nRMSE. Among the various ANN models considered, despite its slightly higher error, Model 2 was considered the optimal model due to the use as input data variables that are commonly measured at ground radiometric stations. The practical advantage of this model lies in the accessibility and availability of GHI,  $\theta_z$ , T,  $k_t$ , and  $\psi$  data, making it easier to implement in real-world scenarios without the need for additional specialized measurements. In contrast, the other models are based on meteorological variables that are not frequently recorded at meteorological stations. ANN Models 3, 7, 8, and 9 depend on CC, which requires the use of a sky camera. Models 1, 4, 5, and 6 rely on DHI, thus requiring the use of a pyrheliometer and a solar tracker, elements of high cost and complex maintenance, and, therefore, scarce in meteorological ground facilities.

**Table 9.** Performance (nRSME (%)) of ANN models of GHUVE, generated from combinations of five and six experimental meteorological variables and from two to six neurons in the hidden layer.

ANN	Number of Variables/Neurons in the Hidden Layer	Meteorological Variables	RSME(%)
Model 1	5/2	GHI, $\theta_z$ , $\epsilon$ , T, $k_t$	14.49
Model 2	5/3	GHI, $\theta_z$ , T, $k_t$ , $\psi$	14.16
Model 3	5/4	GHI, $\theta_z$ , T, CC, $\psi$	13.34
Model 4	5/5	GHI, $\theta_z$ , T, $\Delta$ , $\psi$	13.01
Model 5	6/2	GHI, $\theta_z$ , $k_t$ , $\epsilon$ , T, RH	14.11
Model 6	6/3	GHI, $\theta_z$ , DHI, T, RH, $\psi$	13.59
Model 7	6/4	GHI, $\theta_z$ , T, RH, CC, $\psi$	12.94
Model 8	6/5	GHI, $\theta_z$ , T, RH, CC, $\psi$	12.53
Model 9	6/6	GHI, $\theta_z$ , $k_t$ , T, CC, $\psi$	12.16

### 5. Conclusions

This study was based on the experimental data recorded and analyzed at 10 min intervals between September 2020 and June 2022 in Burgos (Spain). The GHUVE/GHI ratio was analyzed at different time intervals as a function of the sky type classified according to the ISO/CIE standard. The analysis of the GHUVE/GHI ratio yielded a gradual increase from dawn to noon (12:00 h) and a subsequent decrease until sunset. A greater dispersion of values was observed in the central hours of the day (10:00 a.m. to 2:00 p.m.). The relationship showed higher values with a higher dispersion for the months from May until August and lower values in December and January. The value of the ratio and the data dispersion into the three categories (overcast, intermediate, and clear skies) was very similar.

Different models were analyzed to determine GHUVE based on meteorological and radiative variables collected in Burgos, using multilinear regression models (MLR) and artificial neural network (ANN) for all skies, overcast, intermediate, and clear skies. The use of variables from databases or satellite observation was not considered to guarantee, as

far as possible, the applicability of locally obtained models in other locations using data from ground meteorological facilities.

The MLR model fitting results presented high determination coefficients with the experimental data ( $R^2 > 0.92$ ) for all skies, overcast, intermediate, and clear skies. However, the nRMSE value was elevated, exceeding 20% in the four cases. Since the MLR models did not perform as expected, GHUVE was modeled by ANN models, considering the variables used for MLR modeling for each sky type. In all four cases, a good determination coefficient was obtained,  $R^2 > 0.95$ . The nRSME obtained varied between 12 and 21%. The best results were obtained for clear skies ( $R^2 > 0.97$  and nRMSE  $< 12.4\%$ ).

For all skies, the optimal number of variables was evaluated to achieve an nRMSE of less than 15% by means of ANN models. Through the derivation and analysis of multiple models, it was determined that the adequate choice was the model encompassing GHI,  $\theta_z$ , T,  $k_t$ ,  $\psi$ , due to its high performance and the availability of the required inputs from most ground meteorological facilities.

Future research endeavors should incorporate the deeply impactful total ozone column (TOC) variable among the model inputs. Addressing the scarcity of ground-based experimental TOC data could be achieved by using daily interpolated satellite observations. Incorporating other time scales (hourly and daily) and employing corrections based on site adaptation techniques will be imperative to extend the developed models to diverse locations accurately.

**Author Contributions:** Conceptualization, C.A.-T.; Formal analysis, S.G.-R., A.G.-R., D.G.-L. and I.G.; Funding acquisition, C.A.-T.; Investigation, S.G.-R., D.G.-L. and I.G.; Methodology, S.G.-R., A.G.-R. and I.G.; Software, S.G.-R., A.G.-R., D.G.-L. and I.G.; Supervision, C.A.-T.; Validation, C.A.-T.; Visualization, S.G.-R., A.G.-R. and I.G.; Writing—original draft, S.G.-R. and A.G.-R.; Writing—review and editing, C.A.-T. and I.G. All authors have read and agreed to the published version of the manuscript.

**Funding:** This research was funded by MCIN/AEI/ 10.13039/501100011033 and the “European Union Next Generation EU/PRTR grant numbers TED2021-131563B-I00 and PID2022-139477OB-I00 and Junta de Castilla y León, grant number INVESTUN/19/BU/0004.

**Institutional Review Board Statement:** Not applicable.

**Informed Consent Statement:** Not applicable.

**Data Availability Statement:** Copies of the original dataset used in this work can be downloaded from <http://hdl.handle.net/10259/7778> (accessed on 18 September 2023).

**Conflicts of Interest:** The authors declare no conflict of interest.

## Nomenclature

$B_{sc}$	Solar constant (=1361.1 W/m <sup>2</sup> )
CC	Cloud cover (%)
D	Diffuse fraction
DHI	Diffuse horizontal irradiance (W/m <sup>2</sup> )
DNI	Direct normal irradiance (W/m <sup>2</sup> )
GHI	Global horizontal irradiance (W/m <sup>2</sup> )
GHUVE	Global horizontal UV erythemal irradiance (W/m <sup>2</sup> )
$k_t$	Clearness index
$k'_d$	Diffuse to extraterrestrial irradiance
n	Number of data points
nRMSE	Normalized root mean square error (%)
nMBE	Normalized mean bias error (%)
r	Pearson correlation coefficient
RH	Relative humidity (%)
$R^2$	Determination coefficient
T	Air temperature (°C)

TOC	Total ozone column
WS	Wind speed
$\Delta$	Perez's brightness factor
$\varepsilon$	Perez's clearness index
$f_c$	The average value of the orbital eccentricity of the Earth
$\theta_z$	Solar zenith angle (rad)
$\psi$	Solar azimuth angle (rad)

## References

- Ahmed, A.A.M.; Ahmed, M.H.; Saha, S.K.; Ahmed, O.; Sutradhar, A. Optimization algorithms as training approach with hybrid deep learning methods to develop an ultraviolet index forecasting model. *Stoch. Environ. Res. Risk Assess.* **2022**, *36*, 3011–3039. [\[CrossRef\]](#)
- González-Rodríguez, L.; de Oliveira, A.P.; Rodríguez-López, L.; Rosas, J.; Contreras, D.; Baeza, A.C. A Study of UVER in Santiago, Chile Based on Long-Term In Situ Measurements (Five Years) and Empirical Modelling. *Energies* **2021**, *14*, 368. [\[CrossRef\]](#)
- Salvadori, G.; Lista, D.; Burattini, C.; Gugliermetti, L.; Leccese, F.; Bisegna, F. Sun Exposure of Body Districts: Development and Validation of an Algorithm to Predict the Erythral Ultra Violet Dose. *Int. J. Environ. Res. Public Heal.* **2019**, *16*, 3632. [\[CrossRef\]](#) [\[PubMed\]](#)
- Alados-Arboledas, L.; Alados, I.; Foyo-Moreno, I.; Olmo, F.; Alcántara, A. The influence of clouds on surface UV erythral irradiance. *Atmos. Res.* **2003**, *66*, 273–290. [\[CrossRef\]](#)
- Cadet, J.-M.; Portafaix, T.; Bencherif, H.; Lamy, K.; Brogniez, C.; Auriol, F.; Metzger, J.-M.; Boudreault, L.-E.; Wright, C.Y. Inter-Comparison Campaign of Solar UVR Instruments under Clear Sky Conditions at Reunion Island (21° S, 55° E). *Int. J. Environ. Res. Public Health* **2020**, *17*, 2867. [\[CrossRef\]](#)
- Serrano, A.; Antón, M.; Cancillo, M.L.; Mateos, V.L. Daily and annual variations of erythral ultraviolet radiation in Southwestern Spain. *Ann. Geophys.* **2006**, *24*, 427–441. [\[CrossRef\]](#)
- Serrano, M.-A.; Cañada, J.; Moreno, J.C.; Gurrea, G. Solar ultraviolet doses and vitamin D in a northern mid-latitude. *Sci. Total. Environ.* **2017**, *574*, 744–750. [\[CrossRef\]](#)
- Vuilleumier, L.; Harris, T.; Nenes, A.; Backes, C.; Vernez, D. Developing a UV climatology for public health purposes using satellite data. *Environ. Int.* **2021**, *146*, 106177. [\[CrossRef\]](#)
- Human, S.; Bajic, V. Modelling Ultraviolet Irradiance in South Africa. *Radiat. Prot. Dosim.* **2000**, *91*, 181–183. [\[CrossRef\]](#)
- Modenese, A.; Gobba, F.; Paolucci, V.; John, S.M.; Sartorelli, P.; Wittlich, M. Occupational solar UV exposure in construction workers in Italy: Results of a one-month monitoring with personal dosimeters. In Proceedings of the 2020 IEEE International Conference on Environment and Electrical Engineering and 2020 IEEE Industrial and Commercial Power Systems Europe (EEEIC/I&CPS Europe), Madrid, Spain, 9–12 June 2020; pp. 1–5. [\[CrossRef\]](#)
- Vitt, R.; Laschewski, G.; Bais, A.F.; Diémoz, H.; Fountoulakis, I.; Siani, A.-M.; Matzarakis, A. UV-Index Climatology for Europe Based on Satellite Data. *Atmosphere* **2020**, *11*, 727. [\[CrossRef\]](#)
- Utrillas, M.; Marín, M.; Esteve, A.; Salazar, G.; Suárez, H.; Gandía, S.; Martínez-Lozano, J. Relationship between erythral UV and broadband solar irradiance at high altitude in Northwestern Argentina. *Energy* **2018**, *162*, 136–147. [\[CrossRef\]](#)
- Bilbao, J.; Román, R.; Yousif, C.; Mateos, D.; de Miguel, A. Total ozone column, water vapour and aerosol effects on erythral and global solar irradiance in Marsaxlokk, Malta. *Atmos. Environ.* **2014**, *99*, 508–518. [\[CrossRef\]](#)
- ISO/CIE 17166:2019(E); Erythema Reference Action Spectrum and Standard Erythema Dose. ISO: Geneva, Switzerland; CIE: Vienna, Austria, 2019.
- Leal, S.; Tiba, C.; Piacentini, R. Daily UV radiation modeling with the usage of statistical correlations and artificial neural networks. *Renew. Energy* **2011**, *36*, 3337–3344. [\[CrossRef\]](#)
- Esteve, A.R.; Marín, M.J.; Tena, F.; Utrillas, M.P.; Martínez-Lozano, J.A. Influence of cloudiness over the values of erythral radiation in Valencia, Spain. *Int. J. Clim.* **2010**, *30*, 127–136. [\[CrossRef\]](#)
- Bilbao, J.; Mateos, D.; Yousif, C.; Román, R.; De Miguel, A. Influence of cloudiness on erythral solar irradiance in Marsaxlokk, Malta: Two case studies. *Sol. Energy* **2016**, *136*, 475–486. [\[CrossRef\]](#)
- de Miguel, A.; Román, R.; Bilbao, J.; Mateos, D. Evolution of erythral and total shortwave solar radiation in Valladolid, Spain: Effects of atmospheric factors. *J. Atmos. Sol. -Terr. Phys.* **2011**, *73*, 578–586. [\[CrossRef\]](#)
- Bilbao, J.; Román, R.; Yousif, C.; Pérez-Burgos, A.; Mateos, D.; de Miguel, A. Global, diffuse, beam and ultraviolet solar irradiance recorded in Malta and atmospheric component influences under cloudless skies. *Sol. Energy* **2015**, *121*, 131–138. [\[CrossRef\]](#)
- Antón, M.; Serrano, A.; Cancillo, M.; García, J. Influence of the relative optical air mass on ultraviolet erythral irradiance. *J. Atmos. Sol. -Terr. Phys.* **2009**, *71*, 2027–2031. [\[CrossRef\]](#)
- McKenzie, R.L.; Matthews, W.A.; Johnston, P.V. The relationship between erythral UV and ozone, derived from spectral irradiance measurements. *Geophys. Res. Lett.* **1991**, *18*, 2269–2272. [\[CrossRef\]](#)
- Antón, M.; Cazorla, A.; Mateos, D.; Costa, M.J.; Olmo, F.J.; Alados-Arboledas, L. Sensitivity of UV Erythral Radiation to Total Ozone Changes under Different Sky Conditions: Results for Granada, Spain. *Photochem. Photobiol.* **2016**, *92*, 215–219. [\[CrossRef\]](#) [\[PubMed\]](#)



23. Sanchez, G.; Serrano, A.; Cancillo, M.L. Modeling the erythemal surface diffuse irradiance fraction for Badajoz, Spain. *Atmos. Meas. Tech.* **2017**, *17*, 12697–12708. [[CrossRef](#)]
24. Mateos, D.; Bilbao, J.; de Miguel, A.; Pérez-Burgos, A. Dependence of ultraviolet (erythemal and total) radiation and CMF values on total and low cloud covers in Central Spain. *Atmos. Res.* **2010**, *98*, 21–27. [[CrossRef](#)]
25. Bilbao, J.; Román, R.; de Miguel, A.; Mateos, D. Long-term solar erythemal UV irradiance data reconstruction in Spain using a semiempirical method. *J. Geophys. Res. Atmos.* **2011**, *116*, D22211. [[CrossRef](#)]
26. Lindfors, A.; Kaurola, J.; Arola, A.; Koskela, T.; Lakkala, K.; Josefsson, W.; Olseth, J.A.; Johnsen, B. A method for reconstruction of past UV radiation based on radiative transfer modeling: Applied to four stations in northern Europe. *J. Geophys. Res. Earth Surf.* **2007**, *112*, D23201. [[CrossRef](#)]
27. Buntoung, S.; Janjai, S.; Nunez, M.; Choosri, P.; Pratummasoot, N.; Chiwpreecha, K. Sensitivity of erythemal UV/global irradiance ratios to atmospheric parameters: Application for estimating erythemal radiation at four sites in Thailand. *Atmos. Res.* **2014**, *149*, 24–34. [[CrossRef](#)]
28. García-Rodríguez, A.; Granados-López, D.; García-Rodríguez, S.; Díez-Mediavilla, M.; Alonso-Tristán, C. Modelling Photosynthetic Active Radiation (PAR) through meteorological indices under all sky conditions. *Agric. For. Meteorol.* **2021**, *310*, 108627. [[CrossRef](#)]
29. Dieste-Velasco, M.I.; García-Rodríguez, S.; García-Rodríguez, A.; Díez-Mediavilla, M.; Alonso-Tristán, C. Modeling Horizontal Ultraviolet Irradiance for All Sky Conditions by Using Artificial Neural Networks and Regression Models. *Appl. Sci.* **2023**, *13*, 1473. [[CrossRef](#)]
30. Fatima-Ezzahra, D.; Abdellah, B.; Abdellatif, G. Estimation of ultraviolet solar irradiation of semi-arid area—case of Benguerir. In Proceedings of the 2020 International Conference on Electrical and Information Technologies (ICEIT), Rabat, Morocco, 4–7 March 2020; pp. 1–5. [[CrossRef](#)]
31. Alados, I.; Gomera, M.A.; Foyo-Moreno, I.; Alados-Arboledas, L. Neural network for the estimation of UV erythemal irradiance using solar broadband irradiance. *Int. J. Clim.* **2007**, *27*, 1791–1799. [[CrossRef](#)]
32. Barbero, F.J.; López, G.; Batlles, F.J. Determination of daily solar ultraviolet radiation using statistical models and artificial neural networks. *Ann. Geophys.* **2006**, *24*, 2105–2114. [[CrossRef](#)]
33. Jacovides, C.; Tymvios, F.; Boland, J.; Tsitouri, M. Artificial Neural Network models for estimating daily solar global UV, PAR and broadband radiant fluxes in an eastern Mediterranean site. *Atmos. Res.* **2015**, *152*, 138–145. [[CrossRef](#)]
34. Junk, J.; Feister, U.; Helbig, A. Reconstruction of daily solar UV irradiation from 1893 to 2002 in Potsdam, Germany. *Int. J. Biometeorol.* **2007**, *51*, 505–512. [[CrossRef](#)]
35. Feister, U.; Junk, J.; Woltdt, M.; Bais, A.; Helbig, A.; Janouch, M.; Josefsson, W.; Kazantzidis, A.; Lindfors, A.; Outer, P.N.D.; et al. Long-term solar UV radiation reconstructed by ANN modelling with emphasis on spatial characteristics of input data. *Atmos. Meas. Tech.* **2008**, *8*, 3107–3118. [[CrossRef](#)]
36. Malinovic-Milicevic, S.; Vyklyuk, Y.; Radovanovic, M.M.; Petrovic, M.D. Long-term erythemal ultraviolet radiation in Novi Sad (Serbia) reconstructed by neural network modelling. *Int. J. Clim.* **2018**, *38*, 3264–3272. [[CrossRef](#)]
37. Alados, I.; Mellado, J.A.; Ramos, F.; Alados-Arboledas, L. Estimating UV Erythemal Irradiance by Means of Neural Networks. *Photochem. Photobiol.* **2004**, *80*, 351–358. [[CrossRef](#)] [[PubMed](#)]
38. Antón, M.; Cancillo, M.L.; Serrano, A.; García, J.A. A Multiple Regression Analysis Between UV Radiation Measurements at Badajoz and Ozone, Reflectivity and Aerosols Estimated by TOMS. *Phys. Scr.* **2005**, *2005*, 21. [[CrossRef](#)]
39. Kim, J.; Lee, Y.G.; Koo, J.-H.; Lee, H. Relative Contributions of Clouds and Aerosols to Surface Erythemal UV and Global Horizontal Irradiance in Korea. *Energies* **2020**, *13*, 1504. [[CrossRef](#)]
40. Foyo-Moreno, I.; Alados, I.; Alados-Arboledas, L. Adaptation of an empirical model for erythemal ultraviolet irradiance. *Ann. Geophys.* **2007**, *25*, 1499–1508. [[CrossRef](#)]
41. ISO 15469:2004(E)/CIE S 011/E:2003; Spatial Distribution of Daylight—CIE Standard General Sky. *ISO: Geneva, Switzerland*; CIE: Vienna, Austria, 2004.
42. Granados-López, D.; Suárez-García, A.; Díez-Mediavilla, M.; Alonso-Tristán, C. Feature selection for CIE standard sky classification. *Sol. Energy* **2021**, *218*, 95–107. [[CrossRef](#)]
43. Suárez-García, A.; Díez-Mediavilla, M.; Granados-López, D.; González-Peña, D.; Alonso-Tristán, C. Benchmarking of meteorological indices for sky cloudiness classification. *Sol. Energy* **2020**, *195*, 499–513. [[CrossRef](#)]
44. Beyer, H.G.; Martinez, J.P.; Suri, M.T.J.L.; Lorenz, E.; Müller, S.C.; Hoyer-Klick, C.; Ineichen, P. Report on Benchmarking of Radiation Products. Management and Exploitation of Solar Resource Knowledge. In Proceedings of the EUROSUN 2008, 1st International Congress on Heating, Cooling and Buildings, ISES, Lisbon, Portugal, 7–10 October 2008.
45. Gueymard, C.A. Revised composite extraterrestrial spectrum based on recent solar irradiance observations. *Sol. Energy* **2018**, *169*, 434–440. [[CrossRef](#)]
46. Erbs, D.; Klein, S.; Duffie, J. Estimation of the diffuse radiation fraction for hourly, daily and monthly-average global radiation. *Sol. Energy* **1982**, *28*, 293–302. [[CrossRef](#)]
47. Iqbal, M. *An Introduction to Solar Radiation*; Academic Press: New York, NY, USA, 1983. [[CrossRef](#)]
48. Perez, R.; Ineichen, P.; Seals, R.; Michalsky, J.; Stewart, R. Modeling daylight availability and irradiance components from direct and global irradiance. *Sol. Energy* **1990**, *44*, 271–289. [[CrossRef](#)]

49. Gueymard, C.A. A reevaluation of the solar constant based on a 42-year total solar irradiance time series and a reconciliation of spaceborne observations. *Sol. Energy* **2018**, *168*, 2–9.
50. Mukaka, M. Statistics corner: A guide to appropriate use of correlation in medical research. *Malawi MesicL J.* **2012**, *24*, 69–71. [[CrossRef](#)]
51. Heaton, J. *Artificial Intelligence for Humans, Volume 3: Deep Learning and Neural Networks*; Heaton Research, Inc.: St. Louis, MO, USA, 2015.

**Disclaimer/Publisher’s Note:** The statements, opinions and data contained in all publications are solely those of the individual author(s) and contributor(s) and not of MDPI and/or the editor(s). MDPI and/or the editor(s) disclaim responsibility for any injury to people or property resulting from any ideas, methods, instructions or products referred to in the content.